A&A 493, 511–524 (2009)
DOI: 10.1051/0004-6361:200809585

Astronomy & Astrophysics

A kinematic study of the irregular dwarf galaxy NGC 2366 using H I and Hα observations

J. van Eymeren[1,2,3], M. Marcelin[4], B. Koribalski[3], R.-J. Dettmar[2], D. J. Bomans[2], J.-L. Gach[4], and P. Balard[4]

[1] Jodrell Bank Centre for Astrophysics, School of Physics & Astronomy, The University of Manchester, Alan Turing Building, Oxford Road, Manchester, M13 9PL, UK
e-mail: Janine.VanEymeren@manchester.ac.uk
[2] Astronomisches Institut der Ruhr-Universität Bochum, Universitätsstraße 150, 44780 Bochum, Germany
[3] Australia Telescope National Facility, CSIRO, PO Box 76, Epping, NSW 1710, Australia
[4] Laboratoire d'Astrophysique de Marseille, OAMP, Université Aix-Marseille & CNRS, 38 rue Frédéric Joliot-Curie, 13013 Marseille, France

Received 15 February 2008 / Accepted 5 November 2008

ABSTRACT

Context. The metal content of dwarf galaxies and the metal enrichment of the intergalactic medium both suggest that mass loss from galaxies is a significant factor for the chemical evolution history of galaxies, in particular of dwarf galaxies. However, no clear evidence of a blow-away in local dwarf galaxies has been found so far.
Aims. Dwarf galaxies provide a perfect environment for studying feedback processes because their kinematics and their generally low gravitational potential support the long-term survival of shells, filaments, and holes. We therefore performed a detailed kinematic analysis of the neutral and ionised gas in the nearby star-forming irregular dwarf galaxy NGC 2366 in order to make predictions about the fate of the gas and to get a more complete picture of this galaxy.
Methods. A deep Hα image and Fabry-Perot interferometric data of NGC 2366 were obtained. They were complemented by H I synthesis data from the THINGS survey. We searched for line-splitting both in Hα and H I by performing a Gaussian decomposition. To get an idea whether the expansion velocities are high enough for a gas blow-away, we used the pseudo-isothermal halo model, which gives us realistic values for the escape velocities of NGC 2366. The good data quality also allowed us to discuss some peculiarities of the morphology and the dynamics in NGC 2366.
Results. A large red-shifted outflow north west of the giant extragalactic H II region with an expansion velocity of up to 50 km s^{-1} is found in Hα, but not in H I. Additionally, a blue-shifted component north of the giant extragalactic H II region was detected both in Hα and H I with an expansion velocity of up to 30 km s^{-1}. A comparison with the escape velocities of NGC 2366 reveals that the gas does not have enough kinetic energy to leave the gravitational potential.
Conclusions. This result is in good agreement with hydrodynamic simulations and suggests that we need to examine even less massive galaxies ($M_{\rm gas} = 10^6\ M_\odot$).

Key words. galaxies: irregular – galaxies: ISM – galaxies: kinematics and dynamics – galaxies: structure

1. Introduction

Irregular dwarf galaxies are known to be the sites of giant star formation regions. The feedback between massive stars and the interstellar medium (ISM), and on larger scales also the intergalactic medium (IGM), is one of the most important processes in the evolution of these galaxies. Massive stars are strong sources of radiation and mechanical energy. Photoionisation is the most probable mechanism, but also shocks that are produced by stellar winds and supernova (SN) explosions inject huge amounts of energy into the ISM. This leads to numerous ionised gas structures in and around the galactic plane, visible on deep Hα images (e.g., Hunter & Gallagher 1997; Martin 1998; Bomans et al. 1997; van Eymeren et al. 2007). However, ionised gas also exists at kpc distances away from any place of current star formation (Hunter et al. 1993). These structures might be fragmented cool ($T \approx 10^4$ K) shell structures that were left behind by the expanding hot gas (Mac Low & Ferrara 1999), but they can also be explained by turbulent mixing between the hot and the neutral gas (Slavin et al. 1993).

In order to explain the observations, theoretical models were developed in which the gas is shock-heated by collective SNe and accelerated into the ISM forming a thin shell of swept-up ambient gas. Because of Rayleigh-Taylor instabilities the shell can rupture and the hot gas is expelled through tunnel-like features, called chimneys, into the halo of the host galaxy (Norman & Ikeuchi 1989). On the way into the halo and in the halo itself, the gas cools down and depending on the strength of the gravitational potential, the hot gas might fall back onto the galactic disc in the shape of cool clouds, which is described in the *Galactic Fountain* scenario (Shapiro & Field 1976).

In some cases, the gas can be accelerated to velocities beyond the escape velocity of the host galaxy. Especially the relatively low escape velocities of dwarf galaxies will facilitate the removal of substantial amounts of interstellar matter. Therefore, the question comes up whether the gas stays gravitationally bound to the galactic disc (outflow) or whether it can escape from the gravitational potential by becoming a freely flowing wind (galactic wind). Numerical simulations by Mac Low & Ferrara (1999) model superbubble blowout and blow-away in

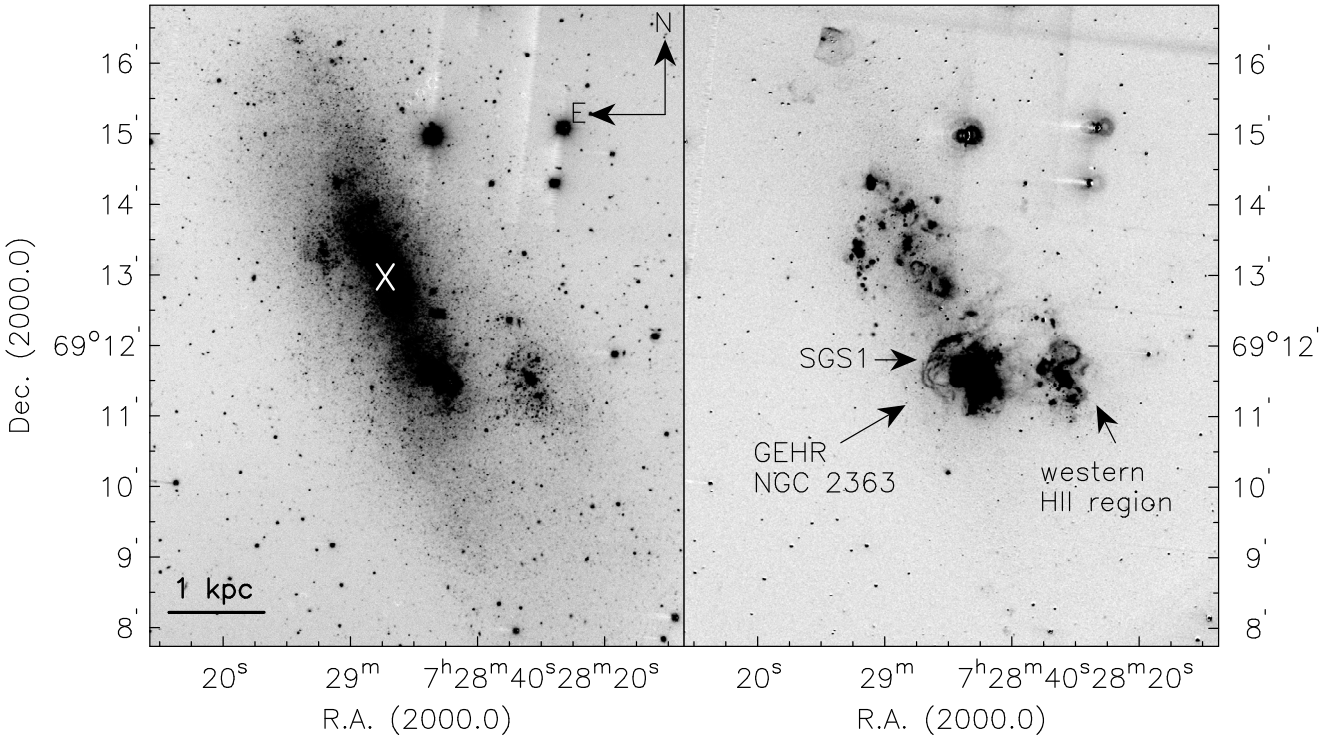

Fig. 1. *R*-band image (*left panel*) and continuum-subtracted Hα image (*right panel*) of NGC 2366. The optical centre is indicated by a white cross on the *R*-band image. The contrast of the Hα image is chosen in a way to emphasise the small-scale structure. The supergiant shell SGS1 (see van Eymeren et al. 2007) as well as two of the main H II regions are marked. In order to stress weaker structures and to differentiate them from the noise, we used adaptive filters based on the H-transform algorithm (Richter et al. 1991).

dark matter dominated dwarf galaxies of different mass and with different energy input. Their models show that only in low mass dwarfs ($M_{\rm gas} = 10^6$ M$_\odot$) a significant fraction of the hot gas can escape from the gravitational potential. The metals however, produced by massive stars and released during a SN explosion, have a high probability to be blown away. The fraction is almost independent of the gas mass or the energy input of the host galaxy.

Therefore, star-forming irregular dwarf galaxies provide a perfect environment to study feedback processes and to hunt for galactic winds. A number of studies already concentrated on the kinematics of ionised gas structures (e.g., Hunter & Gallagher 1997; Martin 1998; van Eymeren et al. 2007), others on the distribution and kinematics of the neutral gas (e.g., Thuan et al. 2004). Only a few studies address both components together in a detailed analysis. Additionally, most authors use single long-slit spectra for the examination of the ionised gas component, which usually only cover some parts of extended target objects. During the last decade, a lot of progress has been made in the field of the so-called 3d spectroscopy. This makes it possible to observe large parts of a galaxy or even the whole galaxy together with sufficient spectral information in one exposure (e.g., Wilcots & Thurow 2001).

In this paper we present a study of the neutral and ionised gas component in the nearby irregular dwarf galaxy NGC 2366. The Hα emission as a tracer of the ionised gas component was observed with a Fabry-Perot (FP) interferometer that provides us with a complete spatial coverage of the stellar disc and relevant spectral information. The FP Hα data are complemented by optical imaging and H I synthesis data.

NGC 2366 is classified as a barred Magellanic-type irregular (IB(s)m) dwarf galaxy (de Vaucouleurs et al. 1991). We adopt a distance of 3.44 Mpc from Tolstoy et al. (1995) that places NGC 2366 in the M 81 group. The nearest neighbour is NGC 2403 at a projected distance of 290 kpc, which makes any kind of recent interaction unlikely. Its appearance in Hα is dominated by the Giant Extragalactic H II Region (GEHR) NGC 2363 in the south-west at $07^{\rm h}28^{\rm m}29.6^{\rm s}$, $+69^{\rm d}11^{\rm m}34^{\rm s}$ (see Fig. 1, right panel) with a luminosity twice as bright as 30 Doradus (Chu & Kennicutt 1994). Recent observations by van Eymeren et al. (2007) revealed the existence of numerous ionised gas structures up to kpc-size, especially close to the GEHR where most of the current star formation activity takes place. Several of them have been shown to expand. The expansion velocities, however, were in all cases much lower than the escape velocities of the galaxy.

This paper is organised as follows: The observations and the data reduction are described in Sect. 2. Section 3 is a comparative description of the Hα and H I morphology. Section 4 presents a kinematic analysis of both Hα and H I data. The results are subsequently discussed in Sect. 5, followed by a short summary in Sect. 6.

2. Observations and data reduction

2.1. Optical imaging

A 900 s *R*-band image and a deep – 3600 s – Hα image of NGC 2366 were obtained on the 16th of October 2007 with the Calar Alto 3.5 m telescope equipped with MOSCA, the Multi Object Spectrograph for Calar Alto. After the standard data reduction performed with the software package IRAF, the continuum image was subtracted to produce an image of the pure Hα line emission. In order to emphasise weaker structures and to differentiate them from the noise, we used adaptive filters based on the H-transform algorithm (Richter et al. 1991). Both images are shown in Fig. 1.

2.2. The Fabry-Perot Hα data

FP interferometry of NGC 2366 was performed on the 1st of March 2006 with the 1.93 m telescope at the Observatoire de Haute-Provence, France. We used the Marseille's scanning FP and the new photon counting camera (Gach et al. 2002). The field of view is $5\farcm8 \times 5\farcm8$ on the 512×512 pixels of the detector and is slightly limited by the interference filter to $5\farcm5 \times 5\farcm5$, which gives a spatial resolution of $0\farcs68$ per pixel. The Hα line was observed through an interference filter centred at the galaxy's rest wavelength of 6564.53 Å with a *FWHM* of 10 Å. The free spectral range of the interferometer – 376 km s^{-1} – was scanned through 24 channels with a sampling step of 15 km s^{-1}. The final spectral resolution as measured from the night sky lines is about 50 km s^{-1}. The seeing was between 3″ and 4″.

60 cycles were observed with an integration time of 10 s per channel, hence 240 s per cycle. After removing bad cycles, a total integration time of 232 min remained. We used a neon lamp for the phase and the wavelength calibration. The data reduction was done with the software package ADHOCw[1], written by Jacques Boulesteix.

2.3. The H I data

We were provided with a fully-reduced data cube from "The H I Nearby Galaxy Survey" (THINGS, Walter et al. 2008), a high spectral and spatial resolution survey of H I emission in 34 nearby galaxies obtained with the VLA in its B, C, and D configuration. The synthesised beam size is $13'' \times 12''$ after using a "natural" weighting. The spectral resolution is 2.6 km s^{-1}. For more details see Walter et al. (2008). We applied a 3-point Hanning smoothing to the cube, which improved the noise level from 0.6 to 0.4 mJy beam^{-1}.

The moment maps were created from the un-smoothed cube by removing all emission below a 2.5σ threshold. The processing and the subsequent analysis of the H I data was performed with GIPSY[2].

3. General morphology

3.1. Results from optical imaging

In addition to the *R*-band and the Hα images presented in Fig. 1, a second grey-scale presentation of the Hα image with a different contrast in order to emphasise the weaker structures is given in Fig. A.1. The galaxy has a bar-like appearance. The main star-forming complex is located at the southern end, coinciding with the GEHR NGC 2363 (Fig. 1, right panel). The H II region west of the GEHR is sometimes referred to as a satellite galaxy (e.g., Drissen et al. 2000). Whether an independent system or not, this H II region is connected to the stellar disc by diffuse, filamentary gas structures.

A catalogue of ionised gas structures can be found in van Eymeren et al. (2007). As the field of view of the Hα image used by van Eymeren et al. (2007) only covered the main part of the stellar disc, we made some new detections on the larger image used here. To the very north of the disc a very interesting structure was found, which is the superbubble SB4 (continuing the labelling of van Eymeren et al. 2007). At the same position, the *R*-band image shows a small cluster of stars. This bubble is remarkable because its morphology consists of a sharply edged shell pointing to the north and a smooth shell pointing south. Additionally, there is a second shell, SB5, heading south-east at a distance of 1 kpc from SB4 without an ionising star cluster nearby. Another peculiarity in NGC 2366 are the very small and faint H II regions that are scattered along the disc on both eastern and western side with no apparent connection to it (see Fig. A.1).

3.2. Results from H I synthesis data

Figure 2 shows the H I channel maps of the cube after applying a 3-point Hanning smoothing, superimposed on a greyscale presentation of our *R*-band image. The white cross in the first channel marks the optical centre of the galaxy. The beam is placed into the lower left corner of the same channel. The corresponding heliocentric velocities are printed in the upper right corner of each channel. The H I emission is very extended (up to a factor of two in comparison to the *R*-band image) and diffuse. The most prominent structure is a tail-like feature at a velocity of 100 km s^{-1}.

The H I moment maps as well as the global intensity profile are displayed in Fig. 3. The H I intensity distribution (upper left panel, 0th moment map) looks very patchy with several intensity maxima in the inner parts and a more diffuse filamentary structure in the outer parts. On a larger scale, the H I forms two bright elongated structures or ridges that are embedded in fainter and smoother gas (see also Hunter et al. 2001; Thuan et al. 2004). Both ridges are parallel to the major axis and the western one coincides with the tail-like feature detected in the channel maps. The total H I flux density is 213 Jy km s^{-1}, which is in good agreement with single dish measurements by, e.g., Thuan & Martin (1981). This shows that the D array of the VLA is very sensitive to extended emission. The H I mass derived from the 0th moment map is given in Table 1.

3.3. A comparison of the neutral and ionised gas distribution

Figure 4 shows a comparison of the ionised and neutral gas distribution in NGC 2366. In the upper panel, the H I contours are overlaid over the continuum-subtracted Hα image. The optical galaxy lies in the centre of the H I distribution, i.e., in the area of highest H I intensity. The H I maximum flux density coincides with the GEHR, the region of currently the strongest star formation in NGC 2366.

For a more detailed study, Fig. 4, lower panel shows an enlargement of the main optical part of NGC 2366. In order to better differentiate between H I maxima and minima, the H I contour at 0.1 Jy beam^{-1} is overlaid in black, the H I intensity contours from 0.15 to 0.4 Jy beam^{-1} in steps of 0.05 Jy beam^{-1} are overlaid in white. First, it can be seen that the H I maximum coinciding with the GEHR is slightly offset from the centre of the Hα emission. The shift is of the order of one beam size or even more and therefore not a resolution effect. Such offsets have also been found in other galaxies like, e.g., IC 10 (Hodge et al. 1994) and are explained by sequential star formation.

Additionally, the arm-like feature in the north-east as well as the western H II region coincide with an H I intensity maximum. And finally, several smaller H I intensity peaks can be found in the northernmost part of NGC 2366, close to but offset from SB4. SB5 seems to be located in an H I hole, which gives rise to the assumption that it expands into the neutral medium by working like a snowplough. The neutral gas in front of the shell is compressed and maybe shock-heated. In the back, a cavity of low densities evolves visible as an H I hole. This phenomenon

[1] http://www.oamp.fr/adhoc/
[2] The Groningen image processing system.

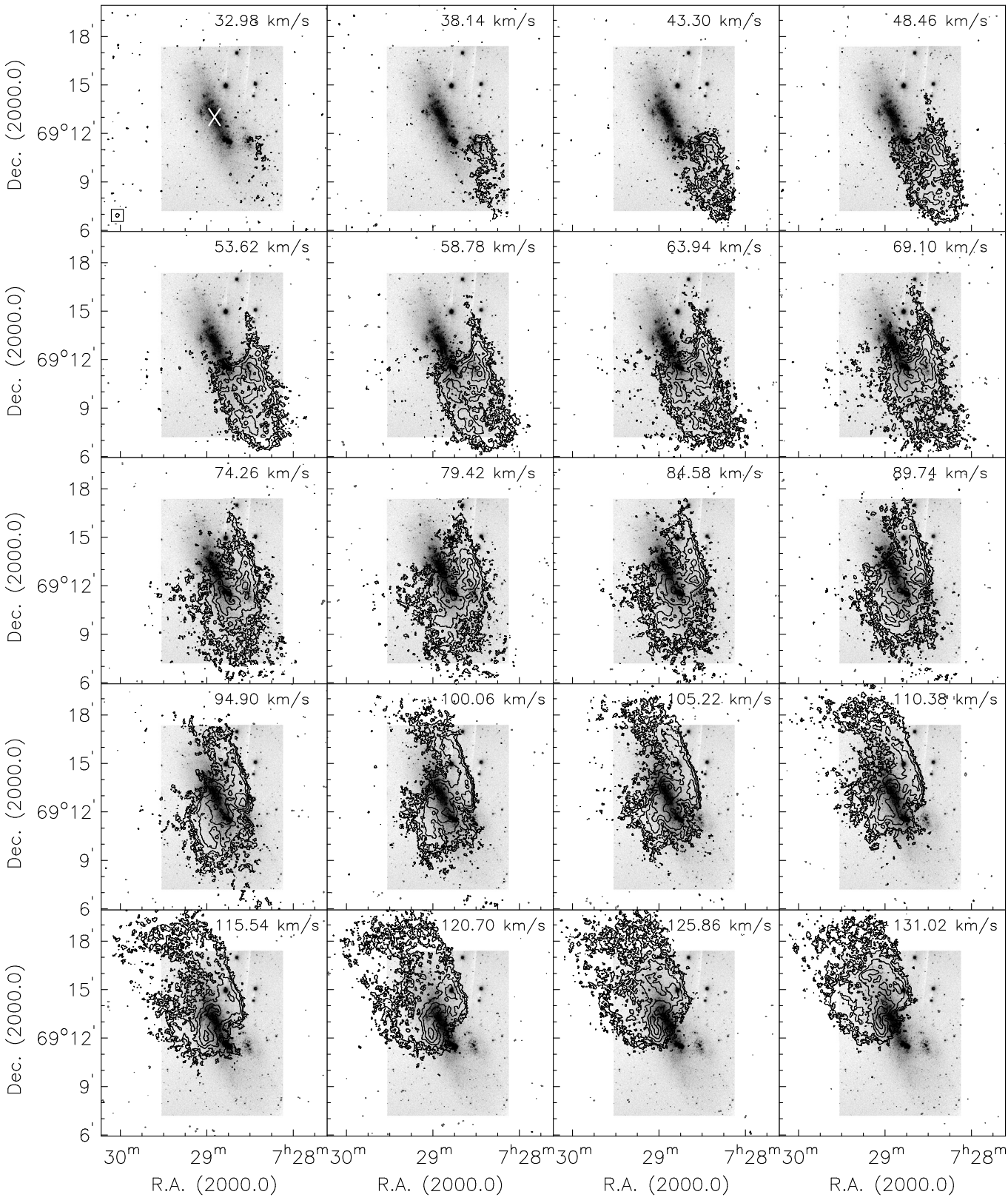

Fig. 2. H I channel maps of NGC 2366 (contours) as obtained from the VLA using "natural" weighting of these data, superposed on the *R*-band image. A 3-point Hanning smoothing was applied to the cube improving the noise level from 0.6 mJy beam^{-1} to 0.4 mJy beam^{-1}. The original channel spacing is 2.6 km s^{-1}. Contours are drawn at -1.2 (-3σ), 1.2 (3σ), 3, 6, 12, and 24 mJy beam^{-1}. The synthesised beam is displayed in the *lower left corner* of the first channel map. The optical centre of the galaxy is marked by a white cross in the same channel map. The corresponding heliocentric velocities are printed in the *upper right corner* of each channel.

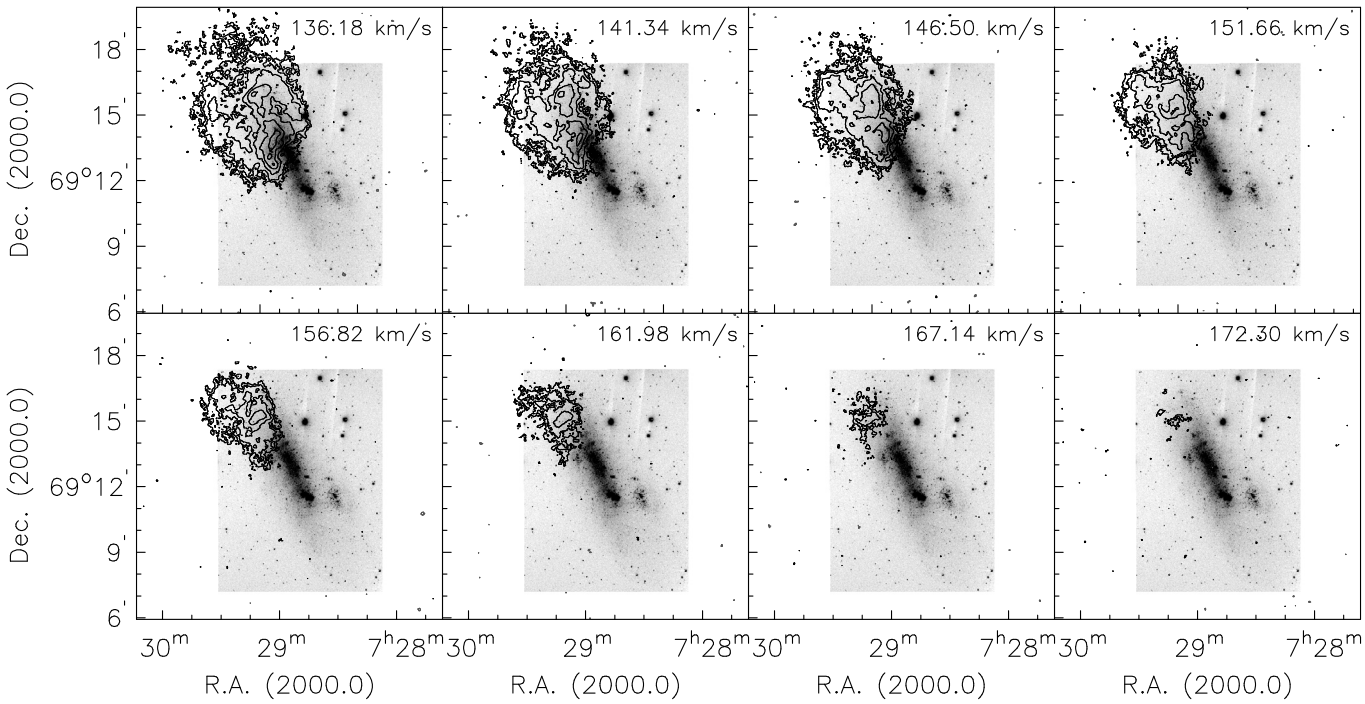

Fig. 2. continued.

cannot be observed in the vicinity of SB4, but the filamentary structures north west of the GEHR are all found in an area of low H I column density (see Sect. 5.1).

4. Kinematic analysis

In this section, we will analyse the kinematics of NGC 2366 in order to study the characteristics of the gas and to explain the peculiarities in its morphology. Spectra extracted from the Hα and the H I data cubes show that both emission lines are sometimes split into several components. Tasks which create velocity fields from a 3d data cube cannot take line-splitting into account. Instead, line-splitting can then even lead to an incorrect measurement of the line properties. Therefore, we performed a Gaussian decomposition by interactively fitting the Hα and H I emission (IRAF task *splot*) in order to measure the characteristics of the lines, especially the peak velocity, and to create the velocity fields from these values. Only detections above a 3σ limit were considered. All given velocities are heliocentric velocities measured along the line of sight.

4.1. The Hα velocity field

The Hα velocity field (Fig. 5, upper panel) shows the component of the strongest intensity. In order to match the seeing and to improve the signal to noise ratio, we summed over 3×3 pixels before performing the Gaussian decomposition. The overall velocity gradient runs from the south-west with velocities of about 65 km s^{-1} to the north-east with velocities of about 120 km s^{-1}. We found two major expanding gas structures (marked in black), a large red-shifted and a faint blue-shifted outflow.

On the lower panel of Fig. 5, we present as an example one of the spectra extracted from the FP data cube (black solid line). The Hα line is split into two components, one at 70 km s^{-1} (blue (dark grey) long-dashed line) and one at 130 km s^{-1} (red (light grey) long-dashed line). The sum of both Gaussian fits is plotted with a green (light grey) short-dashed line and is in good agreement with the observed spectrum. This is one of the spectra extracted from the area of the large red-shifted outflow (marked by a cross in Fig. 5, upper panel). As can be seen, the outflow dominates the Hα profile, whereas the main component is only visible as a wing on the left side. The lines to the left side of the Hα line are night sky lines which could not properly be removed.

This outflow has been detected before by Roy et al. (1991) also using a FP, and by Martin (1998) and van Eymeren et al. (2007) performing long-slit echelle spectroscopy. Roy et al. (1991) concentrated their analysis on the GEHR NGC 2363, Martin (1998) and van Eymeren et al. (2007) were limited by the slit size. E.g., only one slit position by van Eymeren et al. (2007) intersects the outflow, which made it impossible to define its whole extend. This new FP exposure now shows the complete size of the outflow. Assuming a distance of 3.44 Mpc, we estimated a total length of 1.4 kpc, which is two times greater than measured by van Eymeren et al. (2007) and even four times greater than observed by Roy et al. (1991). This length makes it one of the largest outflows ever detected in a dwarf galaxy. The gas expands with a velocity of up to 50 km s^{-1} red-shifted in comparison to the rotational gradient, which is almost a factor of 2 higher than the detections of Roy et al. (1991) and van Eymeren et al. (2007). In case of the observations by Roy et al. (1991), the difference in velocity is most probably due to the fact that they only detected the edge of the outflow where the velocities are lower due to its symmetry. The slit position of van Eymeren et al. (2007) intersects the whole outflow. Here, the discrepancy could be due to their very limited field of view, which did not give them a true Hα rotation curve, or due to their imprecise H I velocity measurements, which they used as a reference value for outflowing gas. The comparison with the H I data presented here will show that the expansion velocity is indeed higher than measured so far (see Sect. 4.4).

The other detected outflow is a faint blue-shifted component north of the GEHR with velocities of 60 to 70 km s^{-1} in

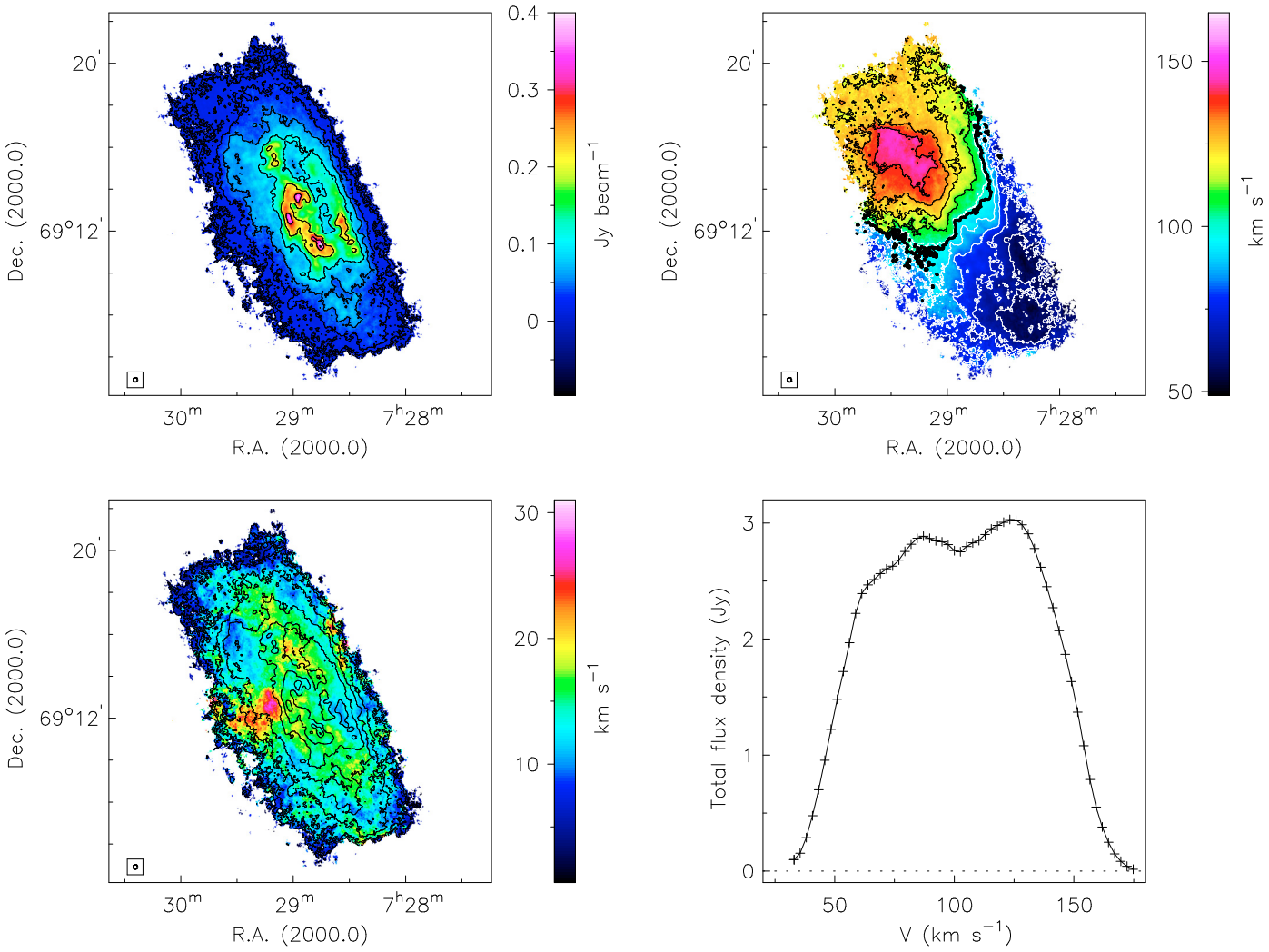

Fig. 3. The H I moment maps of NGC 2366 using "natural" weighting, which leads to a synthesised beam of 13″ ×12″. *Top left*: the H I intensity distribution (0th moment). Contours are drawn at 0.005, 0.01, 0.025, 0.05, 0.1, 0.2, 0.3, 0.4, 0.5, 0.6, and 0.7 Jy beam^{-1} where 5 mJy beam^{-1} correspond to a column density of 3.6×10^{19} atoms cm^{-2}. *Top right*: the H I velocity field (1st moment). Contours are drawn from 40 to 160 km s^{-1} in steps of 10 km s^{-1}. The systemic velocity of 97 km s^{-1} is marked in bold. *Bottom left*: the velocity dispersion (2nd moment), overlaid are the same H I intensity contours as on the 0th moment map. *Bottom right*: the global intensity profile of the galaxy. The short-dashed line marks zero intensity.

comparison to the general velocities of 90 to 100 km s^{-1}, which is discussed in more detail in Sect. 5.1.

As the Hα line is only split in two areas across the galaxy and as the outflow is both times the dominant component, only the main Hα velocity field is shown here.

4.2. The H I velocity field

In order to analyse the general H I kinematics, we worked on the moment maps created with GIPSY (see Sect. 2.3). The H I velocity field (1st moment map), displayed on the upper right panel of Fig. 3, is fairly regular in the inner parts, but disturbed in the outer parts. The velocity gradient goes from the south-west with velocities of about 60 km s^{-1} to the north-east with velocities of about 145 km s^{-1}, which is similar to the Hα velocity gradient. The isovelocity contours close at both ends of the galaxy, which might be caused by the bar and possibly by a warp structure in the outer part. Especially the north-western part shows a completely different kinematic behaviour to what is expected from a regularly rotating galaxy.

The velocity dispersion map (Fig. 3, lower left panel, 2nd moment) varies between 10 km s^{-1} in the outer parts and 17 km s^{-1} in the inner parts of NGC 2366. The dispersion peaks with values of up to 28 km s^{-1} in an area east of the optical disc which is also clearly offset from any H I maximum. Close to the Hα shell SB4 in the north, a very small H I dispersion peak can be seen with a maximum value of 25 km s^{-1}, which is again offset from a nearby H I maximum. This is not unusual as a high velocity dispersion suggests a high level of turbulence which will naturally decrease the H I column densities. The high H I velocity dispersions on the western and eastern edges of the galaxy have to be treated with care. A closer look at the H I velocities in these areas will show that this is an effect of low signal to noise (see Sect. 4.4).

4.3. The H I rotation curve

In order to investigate the fate of the gas, we need to know some of the kinematic parameters of NGC 2366 like its inclination or its rotation velocity. Therefore, we derived a rotation curve from

Table 1. H I properties measured from the THINGS data.

Parameters [Unit]	NGC 2366
optical centre[a]:	
α (J2000.0)	$07^h28^m54.6^s$
δ (J2000.0)	+69° 12′ 57″
D [Mpc][b]	3.44
dynamic centre[c]:	
α (J2000.0)	$07^h28^m55.4^s$
δ (J2000.0)	+69° 12′ 27″
v_{sys} [km s^{-1}][c]	97
i [°][c]	64
PA [°][c]	45
v_{rot} [km s^{-1}][c]	50
F_{HI} [Jy km s^{-1}]	213
M_{HI} [10^8 $M_\odot$]	5.95
H I diameter [′]	15 × 7
" [kpc]	15 × 7
H I / opt. ratio	1.9 × 2.8
$\langle\sigma\rangle$ [km s^{-1}]	10 / 17
σ_{Peak} [km s^{-1}]	28.2
$r_{HI,max}$ [kpc]	7.5
M_{dyn} [10^9 $M_\odot$]	4.3

[a] Data from NED; [b] distance measured from cepheids (Tolstoy et al. 1995); [c] derived by fitting a tilted-ring model to the H I data.

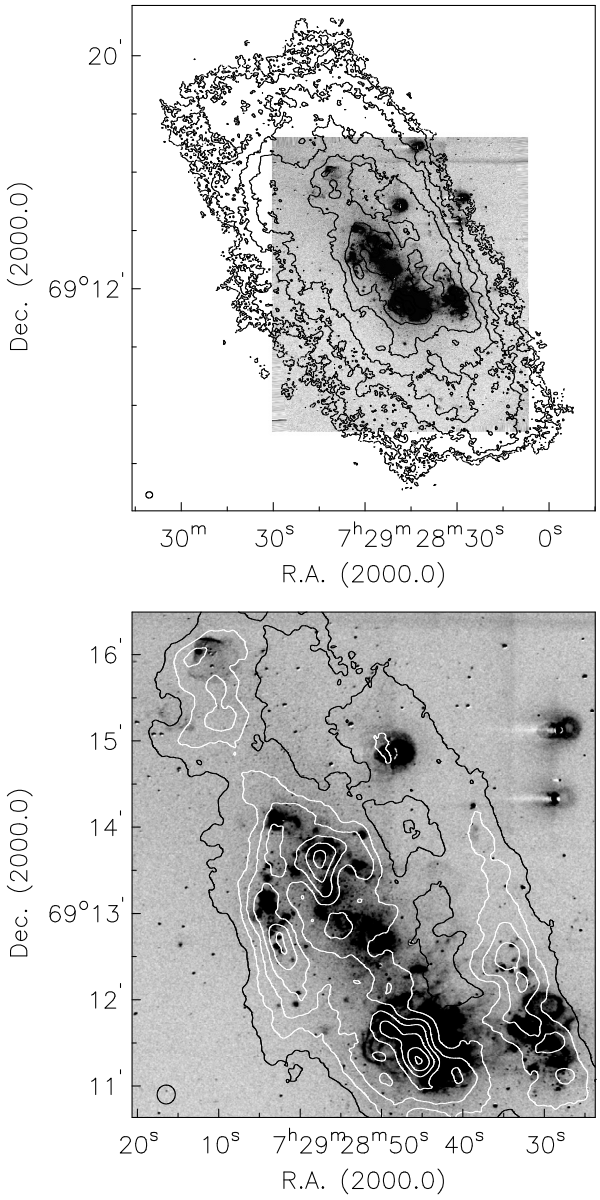

Fig. 4. A comparison of the Hα and H I morphology. The *upper panel* shows the continuum-subtracted Hα image. Overlaid in black are the H I intensity contours at 0.005, 0.01, 0.025, 0.05, 0.1, 0.2, 0.3, and 0.4 Jy beam^{-1}. The *lower panel* displays an enlargement of the optical part. The H I contour at 0.1 Jy beam^{-1} is overlaid in black, the H I intensity contours from 0.15 to 0.4 Jy beam^{-1} in steps of 0.05 Jy beam^{-1} are overlaid in white, which allows us to distinguish between maxima and minima in the neutral gas distribution.

the H I data by fitting a tilted-ring model to the observed velocity field. Figure 6, upper left panel shows the resulting curves.

At the beginning, initial estimates for the kinematic parameters had to be defined, which were obtained by interactively fitting ellipses to the H I intensity distribution using the GIPSY task *ellfit*. These were then used as an input for the tilted-ring fitting routine *rotcur*. The width of the rings was chosen to be half the spatial resolution, i.e., 6″ in this case. In order to get the most precise values, three different approaches were made by always combining receding and approaching side. First, the initial estimates were all kept fixed. The resulting curve is indicated by the green (light grey) symbols in Fig. 6, upper left panel. In a second approach, the parameters were iteratively defined for all rings. Up to a radius of 300″, which corresponds to a distance of 5 kpc from the dynamic centre, no significant deviation or a sudden change of any of the parameters was noticed so that an average value (given in Table 1) was taken for each parameter (black symbols). In this case, a rotation curve was also measured for receding and approaching side alone, indicated by the error bars of the black symbols. As a last approach, the so derived parameters were all kept free in order to reproduce the result of the second approach (red (dark grey) symbols).

The green (light grey) symbols are in very good agreement with the black ones over the whole range of 450″. The red (dark grey) symbols follow the black and green (light grey) ones up to a radius of 200″. Beyond a radius of 300″, the deviation is of the order of 30 to 40 km s^{-1} and the differences between receding and approaching side become larger. The reason for this is that the filling factors of the rings drop from about 1 to about 0.5 at a radius of 300″ as the galaxy does not have a clear elliptical shape. This leads to a higher uncertainty in calculating the rotation velocity. Therefore, all values above this radius have to be treated with care.

In general, the shape of the derived rotation curve fits the ones expected for a dwarf galaxy. In the inner 100″ the velocity gradient is very steep and linear, indicating solid body rotation, which is a characteristic sign of dwarf galaxies. From 100″ to 200″ the curve is still linear, but less steep coming to a plateau at 220″. From 320″ on, the rotation curve declines, which has already been implied by the closing velocity contours in the 1st moment map (Fig. 3, upper right panel).

The best-fitting parameters derived in the iterative approach are given in Table 1. The systemic velocity of 97 km s^{-1} is in good agreement with the values measured by Hunter et al. (2001) and Thuan et al. (2004) (99 and 101 km s^{-1}, respectively). We derived an inclination of 64° and a position angle of 45° in comparison to i = 65° and PA = 46° published by, e.g., Hunter et al. (2001). Our derived rotation velocity of 50 km s^{-1} is also in very

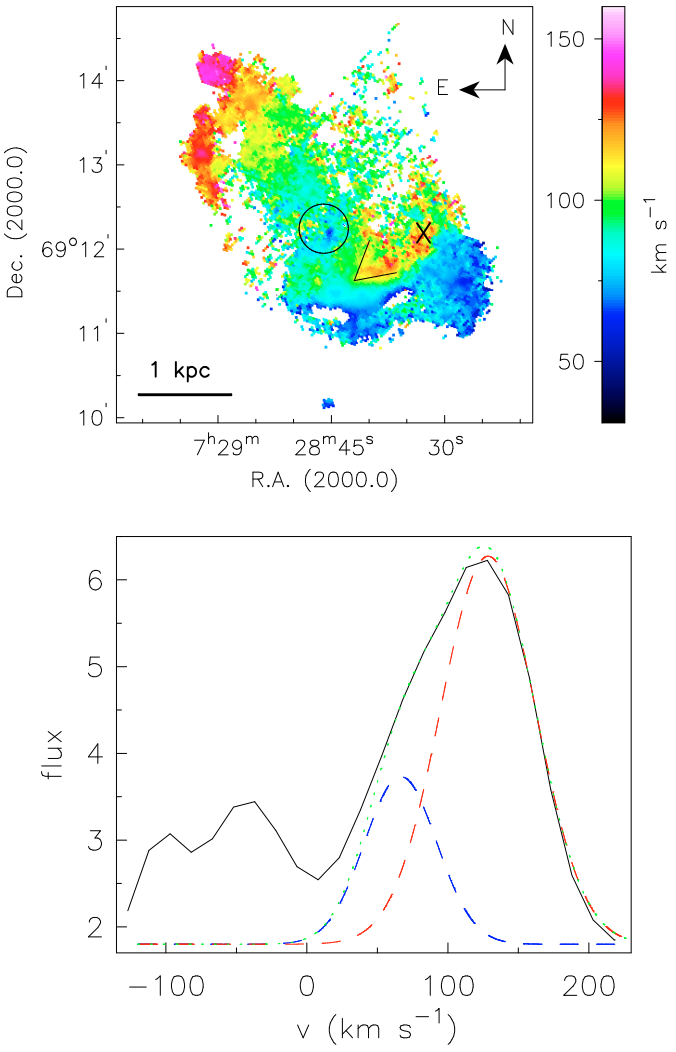

Fig. 5. The Hα velocity field of NGC 2366. The *upper panel* shows the velocity field of the strongest component. The positions of the two detected outflows are marked. The *lower panel* displays one example spectrum (black solid line) which was extracted from the FP data cube at the position of the huge red-shifted outflow (black cross in the Hα velocity field) and which shows the flux in arbitrary units *vs.* the velocity offset (not corrected for the systemic velocity of NGC 2366). The Hα line is split into a component at 70 km s^{-1} (blue (dark grey) long-dashed line) and one at 130 km s^{-1} (red (light grey) long-dashed line). The sum of both Gaussian fits is plotted with a green (light grey) short-dashed line.

good agreement with the values measured, e.g., by Hunter et al. (2001) of 47 km s^{-1}.

In order to prove the reliability of the derived parameters, a model velocity field with the best-fitting parameters was created using the GIPSY task *velfi* (Fig. 6, lower left panel) and subtracted from the original velocity map (upper right panel). The residual map can be seen in Fig. 6, lower right panel. Overlaid in black is the outermost H I intensity contour. The overall velocity field is well represented by our derived parameters except for the outer parts in the north-west and south-east. Here, the residuals reach values of more than 20 km s^{-1} in comparison to a general value of ±10 km s^{-1}. The north-western part could not be fitted with this model.

4.4. A comparison of the neutral and ionised gas kinematics

The Hα velocity field (see Fig. 5) shows two major deviations from the overall rotation velocity, a red-shifted component north west of the GEHR and a blue-shifted one north of the GEHR. As a next step, the H I velocity field was subtracted from the Hα velocity field. Therefore, the FP data were smoothed to fit the H I spatial resolution of 13″ × 12″. The residual map is shown in Fig. 7. At most positions, the velocities of the neutral and ionised gas are in good agreement with offsets of less than ±10 km s^{-1}. The large red-shifted outflow clearly stands out with an expansion velocity of up to 50 km s^{-1}. Additionally, the whole northern part except for the arm-like feature to the east seems to have a faint blue-shifted component with an offset maximum of 30 km s^{-1} and a median offset of 15 km s^{-1}. This expanding gas could already be seen on the original Hα velocity map. It coincides with an area of diffuse and filamentary emission between the GEHR and the northern tail (see Fig. 4, lower panel). For a detailed catalogue of the single filaments see van Eymeren et al. (2007), their Fig. A.1 and Table A1.

In order to look closer at the H I kinematics in the area of the expanding ionised gas and to check the regions of high H I velocity dispersion, we performed a Gaussian decomposition of the H I data as described above. The result is shown in Fig. 8 and some example spectra extracted from the H I cube are given in Fig. 9 together with the fitted Gaussian profiles for the single components (long-dashed blue (dark grey) and red (light grey) lines) and the resulting sum (short-dashed green (light grey) lines). The velocities were averaged over one beam size, which is in this case roughly 12″ in both spatial directions. The strongest component is presented in the middle panel. Overlaid in white are the H I velocity dispersion contours at 20 and 25 km s^{-1} and the outer Hα intensity contour in black. For a comparison, the blue- and red-shifted components are shown on the left and right panel. Note that regions where we did not find a blue- or red-shifted component were filled with the main component.

Figure 10 shows an enlargement of SB4 and the area of the GEHR. Overlaid over the three H I velocity components are some of the Hα intensity contours. The superbubble SB4, the supergiant shell SGS1 (see Fig. 1), and the outflow OF are marked. As already mentioned in Sect. 3.3, the huge outflow north west of the GEHR expands into an area of low column density (a factor of at least two lower than the surroundings). The H I velocity maps in Fig. 10, lower row show no line-splitting, which can also be seen by looking at a spectrum in this area (Fig. 9, panel d). Only close to the origin of the outflow, a second component appears in the H I line profile. With a velocity of 100 km s^{-1} in comparison to the outflow velocity of 130 km s^{-1}, it is most probably not connected to the outflow.

SB4 has also no counterpart in H I (see Fig. 10, upper row). The same is true for SGS1 (lower row). Line-splitting of the H I emission takes place in the north-eastern part of the GEHR going to the south, which is at the position of the ridge mentioned by Hunter et al. (2001) or Thuan et al. (2004). This is discussed in more detail in Sect. 5.3.

Finally, a hint of the faint blue-shifted component detected on the Hα velocity map (see Fig. 5) is also visible in H I with the same velocity of 65 km s^{-1} (see Fig. 9, panel c).

5. Discussion

Our analysis has shown that NGC 2366 harbours many interesting features both in its gas distribution and its gas kinematics. In the following subsections, we try to explain the detections (and

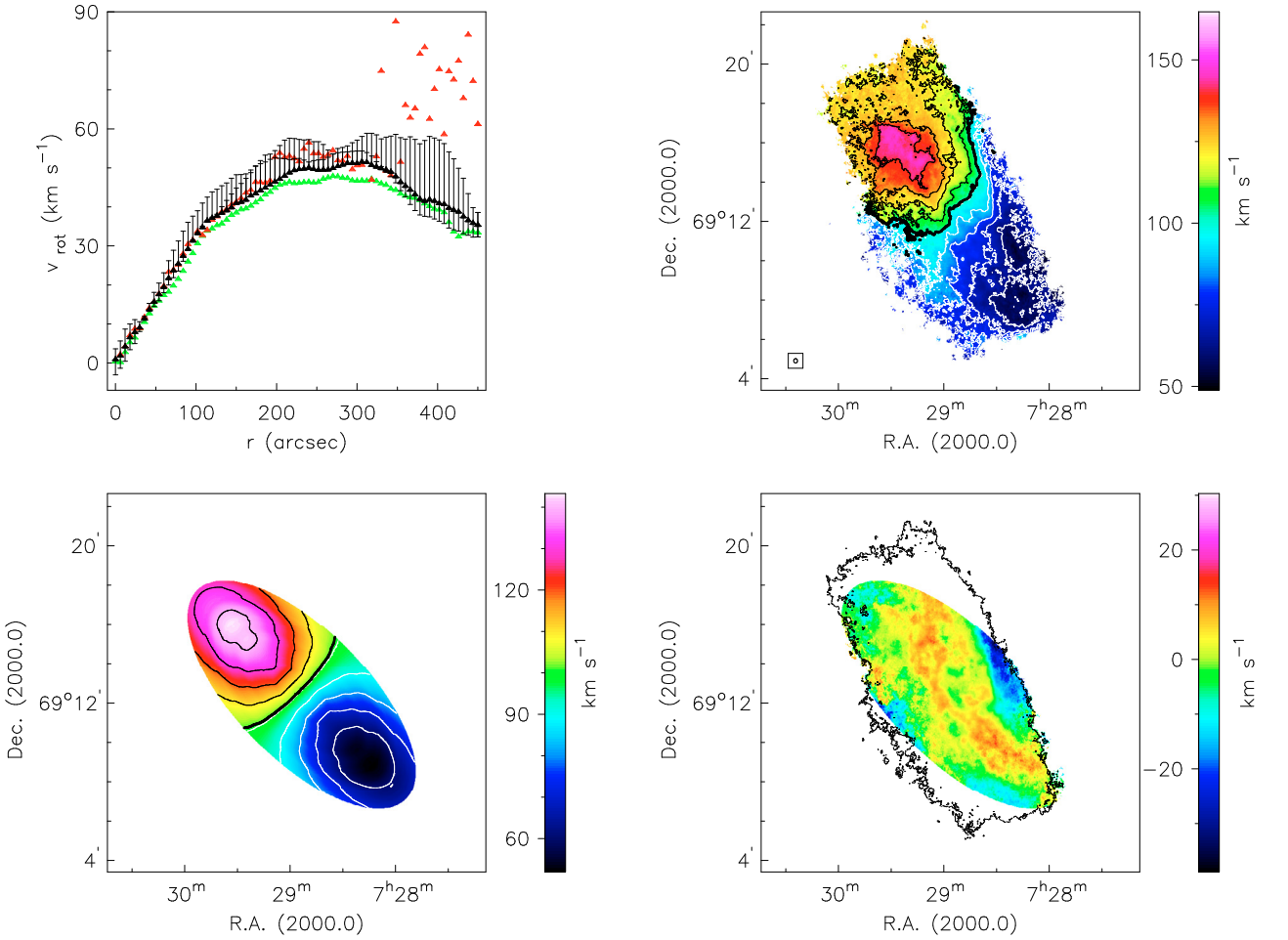

Fig. 6. The H I kinematics of NGC 2366. *Top left*: the rotation curve derived from performing a tilted-ring analysis. Different approaches were chosen: the black symbols represent the best-fitting parameters, the error bars indicate receding and approaching side, respectively. The green (light grey) curve was derived by taking the initial estimates and keep them fixed, the red (dark grey) curve by taking the best-fitting parameters and let them vary. *Top right*: the observed H I velocity field. *Bottom left*: the model velocity field, based on the best-fitting parameters. *Bottom right*: the residual map after subtracting the model from the original velocity map. The outermost H I intensity contour at 0.005 Jy beam^{-1} is overlaid in black.

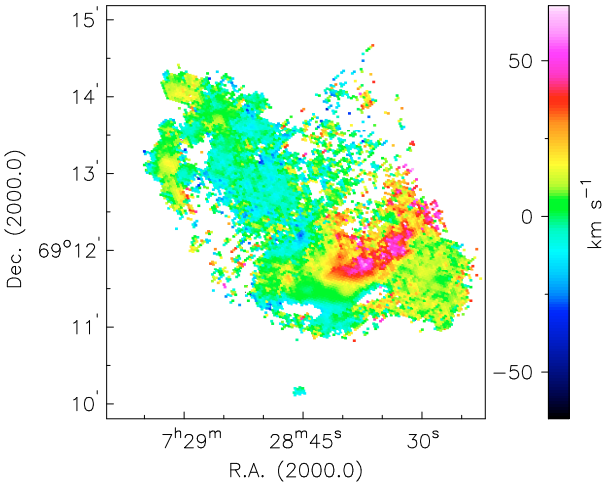

Fig. 7. A comparison of the neutral and ionised gas kinematics. The residuals after subtracting the H I velocity field from the Hα velocity field are shown.

also a non-detection) and deal with the important question what the fate of the outflows is.

5.1. The outflows

Two major outflows were found in the Hα velocity field. The large red-shifted outflow expanding from the GEHR to the north-west is not detected on the H I velocity map, whereas the blue-shifted outflow north of the GEHR has a counterpart in H I. Additionally, we see shell-like structures (SGS1, SB4) on the Hα image with no kinematic evidence on the H I map. Resolution effects cannot be responsible for the non-detection as the structures cover a field of several beam sizes. Unfortunately, we cannot trace the shells in the Hα velocity field as SB4 lies outside the field of view and SGS1 is covered by artificial emission caused in the detector (see Sect. 5.2). However, we have already shown that SGS1 is kinematically visible on long-slit echelle spectra (van Eymeren et al. 2007).

The question which now arises is why the blue-shifted outflow is detected both in Hα and H I, whereas the red-shifted outflow is only detected in Hα. This is probably an effect of age and energy input. Considering their position in the galaxy, it can be assumed that both outflows have a different origin. The large red-shifted outflow is most probably driven by the two large star clusters in the GEHR (Drissen et al. 2001). Assuming a deprojected distance from the two central star clusters of approximately 1 kpc and a constant expansion velocity of 50 km s^{-1},

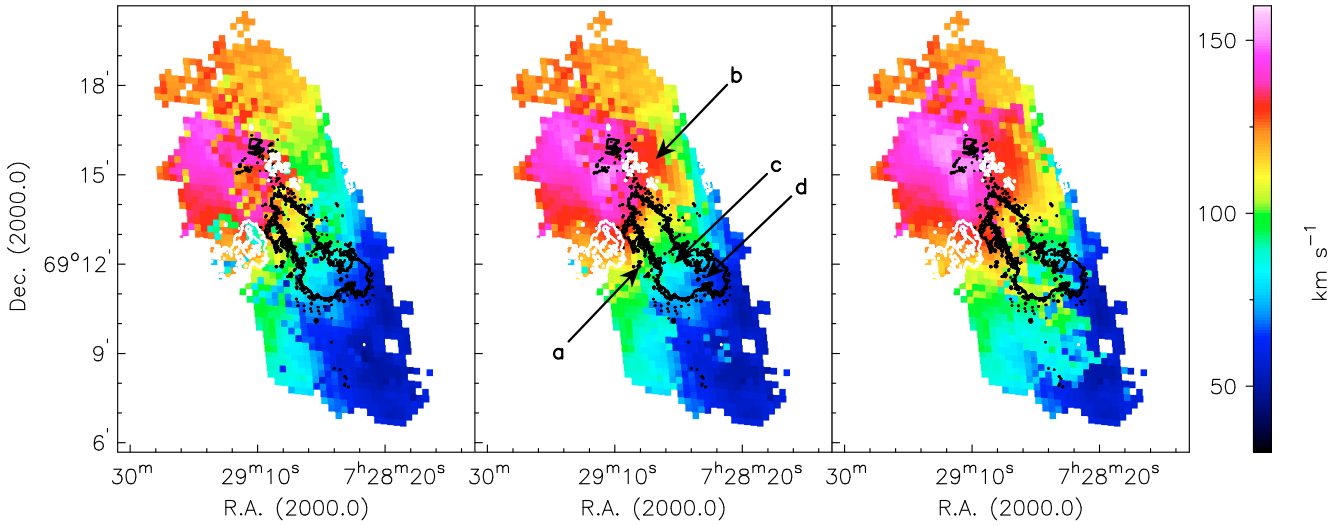

Fig. 8. Gaussian decomposition of the H I line. Blue-shifted (*left panel*), main (*middle panel*) and red-shifted (*right panel*) components of the H I velocities are shown. Overlaid in white are the H I velocity dispersion contours at 20 and 25 km s^{-1} together with the outermost Hα intensity contour in black. The positions of the four spectra shown in the next figure are indicated.

we can estimate the expansion time of the red-shifted outflow to be 2×10^7 yr. According to Drissen et al. (2001), the older star cluster has an age of 3 to 5 Myr. This means that the outflow must originate from a former star formation event and is now driven further out by the new event. The estimated cooling times for both outflows (see Martin 1998) lie clearly above the expansion ages so that radiative losses can be neglected. Therefore, the gas could already have been fully ionised by the former event. On the other hand, it is also possible that our assumption of a constant expansion is wrong. The expansion into a dense environment could have caused a decline in the expansion velocity of the gas over the expansion time. A continued decline would of course have strong consequences for the fate of the gas.

The blue-shifted gas probably gets its energy from a star cluster north of the GEHR. Assuming a distance of 500 pc and again a constant expansion velocity, this time of 30 km s^{-1}, the expansion time is comparable to the one of the huge red-shifted outflow. As the age of this star cluster is not known, we cannot tell whether it is alone responsible for the blue-shifted outflow. What we can tell is that because of the comparable expansion ages, the energy input for the blue-shifted component must have been lower or the neutral gas densities higher, as the gas is not fully ionised, yet. Furthermore, the fact that we can only detect a blue-shifted component does not necessarily exclude the existence of a red-shifted component. A detection depends on the column density. In this case, it could be possible that the blue-shifted gas runs into an area of higher column-density, whereas the red-shifted part expands into an area of lower column density. The same could be true for the large red-shifted outflow. Here, we do not see a blue-shifted component in Hα and we do not see any counterpart in H I. Possibly, the energy input was so strong that all the gas was immediately ionised, e.g., by shock heating. The expansion velocities are almost twice the velocities of the blue-shifted outflow. The low H I column density in comparison to its surroundings also suggests that high amounts of neutral gas have already been ionised.

Both processes, ionisation of the neutral gas and blowout should affect a smooth H I intensity distribution. Figure 11 shows the central region of the 1st moment map. As already mentioned in Sect. 3.2, the intensity distribution is quite patchy. At several locations associated with filamentary and shell-like structure in Hα, we see small holes in the H I distribution indicated by red (light grey) ellipses. These H I holes are often close to the observed outflows. Especially the large red-shifted outflow is expanding into an area of very low H I column density.

In order to complete the discussion of the gas kinematics and the morphology, the hot ionised gas has to be included, too. For NGC 2366 ROSAT and XMM Newton data are available. Stevens & Strickland (1998) analysed the ROSAT data which show that if there is X-ray emission associated with NGC 2366, it is barely detectable. The same is true for the XMM image where we might see faint X-ray emission in the centre of the GEHR (which is to be expected as it is the main area of current star formation activity) as well as in the northern part. However, no strong source associated with NGC 2366 could be detected.

5.2. Superbubble blowout in NGC 2366?

As already mentioned in Sect. 4.1, Roy et al. (1991) observed NGC 2366 with a FP interferometer centred on [O III] λ5007. Their velocity field shows line-splitting only within the GEHR NGC 2363. Next to the huge outflow they also reported the detection of an expanding superbubble around NGC 2363 with a diameter of 200 pc and an expansion velocity of 45 km s^{-1}. Echelle spectroscopy of the central region performed by Martin (1998) and van Eymeren et al. (2007) revealed neither a blue- nor a red-shifted component close to the centre of NGC 2363. The bubble is also not visible in the H I velocity field (see Fig. 10).

During the analysis of our FP data, we looked very carefully at the GEHR. What we found is that not only in this but also in other galaxies, the FP observations of bright emission line regions, e.g., of GEHRs, seem to be affected by blurring inside the detector. This leads to an unusually high, artificial velocity gradient in these emission line regions. In NGC 2366, e.g., the blurring caused a velocity gradient of more than 200 km s^{-1} within 1 kpc. This is unphysical in comparison to the slowly rising velocity gradient in the other parts of the galaxy and is not observed in H I. Assuming that this gradient comes from true emission, its interpretation as an expanding superbubble is indeed intimating. Therefore, we suppose that most probably, Roy et al. (1991)

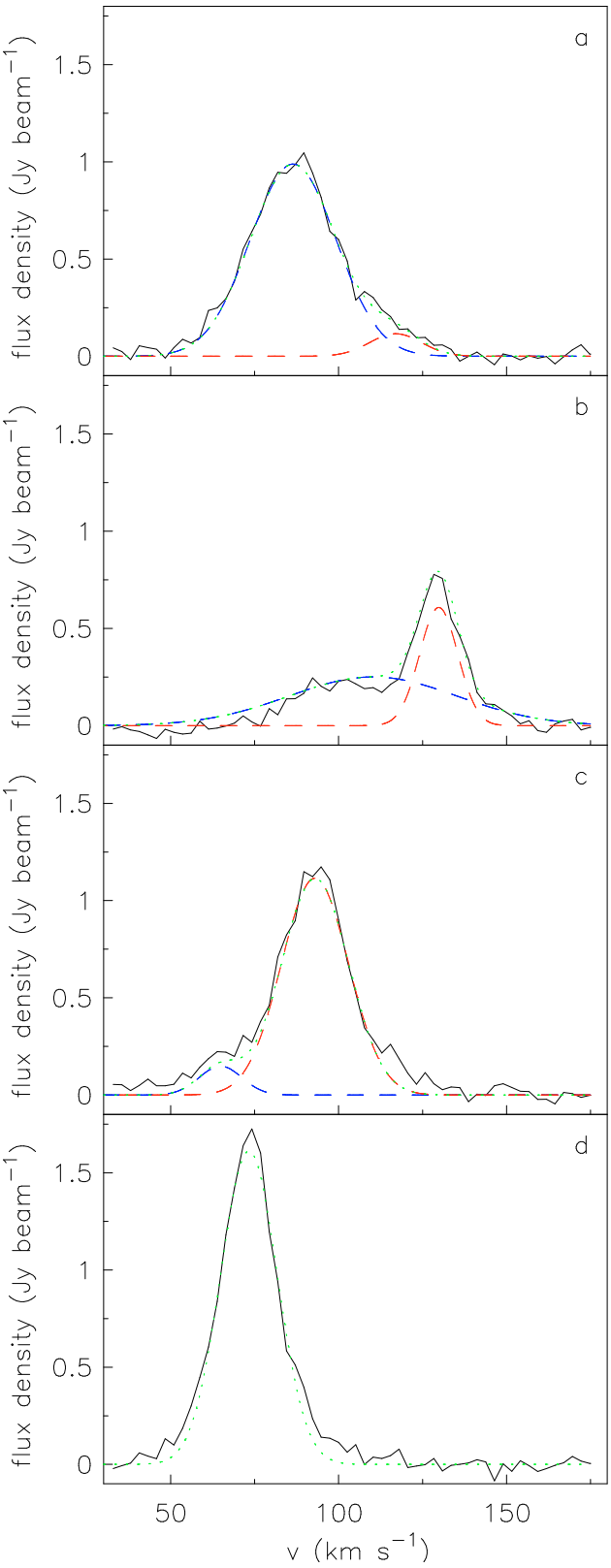

Fig. 9. Some examples of H I line profiles. The Gaussian profiles fitted to the single components are plotted with blue (dark grey) long-dashed lines and red (light grey) long-dashed lines, the resulting sum of the profiles is displayed with a green (light grey) short-dashed line. **a)** The eastern ridge with an additional red-shifted component. **b)** The western ridge with an additional blue-shifted component. **c)** A hint of the blue-shifted component north of the GEHR with $v_{\rm helio}$ = 65 km s^{-1}. **d)** The red-shifted outflow north-west of the GEHR with $v_{\rm helio}$ = 130 km s^{-1} is not detected in H I.

interpreted an artefact as a real expanding bubble as they were not aware of the technical problem of blurring inside the detector. They could also have been biased by a saturation problem of the photon counting system, leading to an artificial splitting of the observed emission line.

5.3. Spiral arm structure in NGC 2366

NGC 2366 shows several peculiarities. Photometric HST observations by Tikhonov & Galazutdinova (2008) reveal an overdensity of blue stars at a galactocentric distance of 0.9 kpc against the overall decrease in the young-star number density with galactocentric distance, which has also been suggested by a B/V presentation by Hunter & Elmegreen (2006). At the same distance, our H I observations as well as the ones by Hunter et al. (2001) and Thuan et al. (2004) show the presence of two parallel ridges running along the major axis. Another peculiarity is the H II complex west of the GEHR, which is often referred to as a satellite galaxy interacting with NGC 2366 (e.g., Drissen et al. 2000).

Tikhonov & Galazutdinova (2008) suggest from their results of the stellar photometry that the H I ridges, interpreted as a deprojected H I ring by Hunter et al. (2001) and Thuan et al. (2004), could be weak spiral arms. Our multi-wavelength study gives further evidence for the existence of two weak spiral arms in NGC 2366, one located at the eastern part of the stellar disc and one at the western side (see Fig. A.1). In Hα, the spiral arms can be traced by an alignment of small isolated H II regions at large distances from the disc. The most distinct ones (numbered 7 and 8) are 2.7 and 3 kpc away from the disc (see also Hunter et al. 2001).

Looking again at the enlarged view of the central region (Fig. 4), we see maxima in the H I column density that follow the spiral arms out of the disc. This could indeed be explained as a concentration of neutral gas formed by a density wave going through the galaxy. All along the spiral arms, the H I line is split into two components, which has already been mentioned by, e.g., Thuan et al. (2004). A closer look at the H I velocities (Fig. 8) shows that next to the main component, a red-shifted component runs along the eastern arm to the south and a blue-shifted component along the western arm to the north (see also the example spectra in Fig. 9, panels a and b). The eastern arm crosses the supergiant shell SGS1. As the red-shifted component is visible on large scales, it is unlikely that we can see an additional red-shifted component belonging to the SGS1.

Furthermore, we compared our data to the GALEX FUV image of NGC 2366 (Gil de Paz & Madore 2005) where the star distribution is more pronounced than on the Hα image. It also suggests the existence of two weak spiral arms, which coincide with the H I ridges and the small H II regions.

Taking all this together, we can confirm the conclusion of Tikhonov & Galazutdinova (2008) that NGC 2366 seems to be a weak two-armed spiral.

5.4. Outflow or galactic wind?

We found two main expanding gas structures in NGC 2366. One is only visible in Hα with an expansion velocity of 50 km s^{-1}, the other one shows similar expansion velocities in Hα and H I of 30 km s^{-1}. Both were probably driven by a former star formation event.

We now want to make some statements about the fate of the gas by comparing the expansion velocities of the outflows to the escape velocities of NGC 2366. As dwarf galaxies are

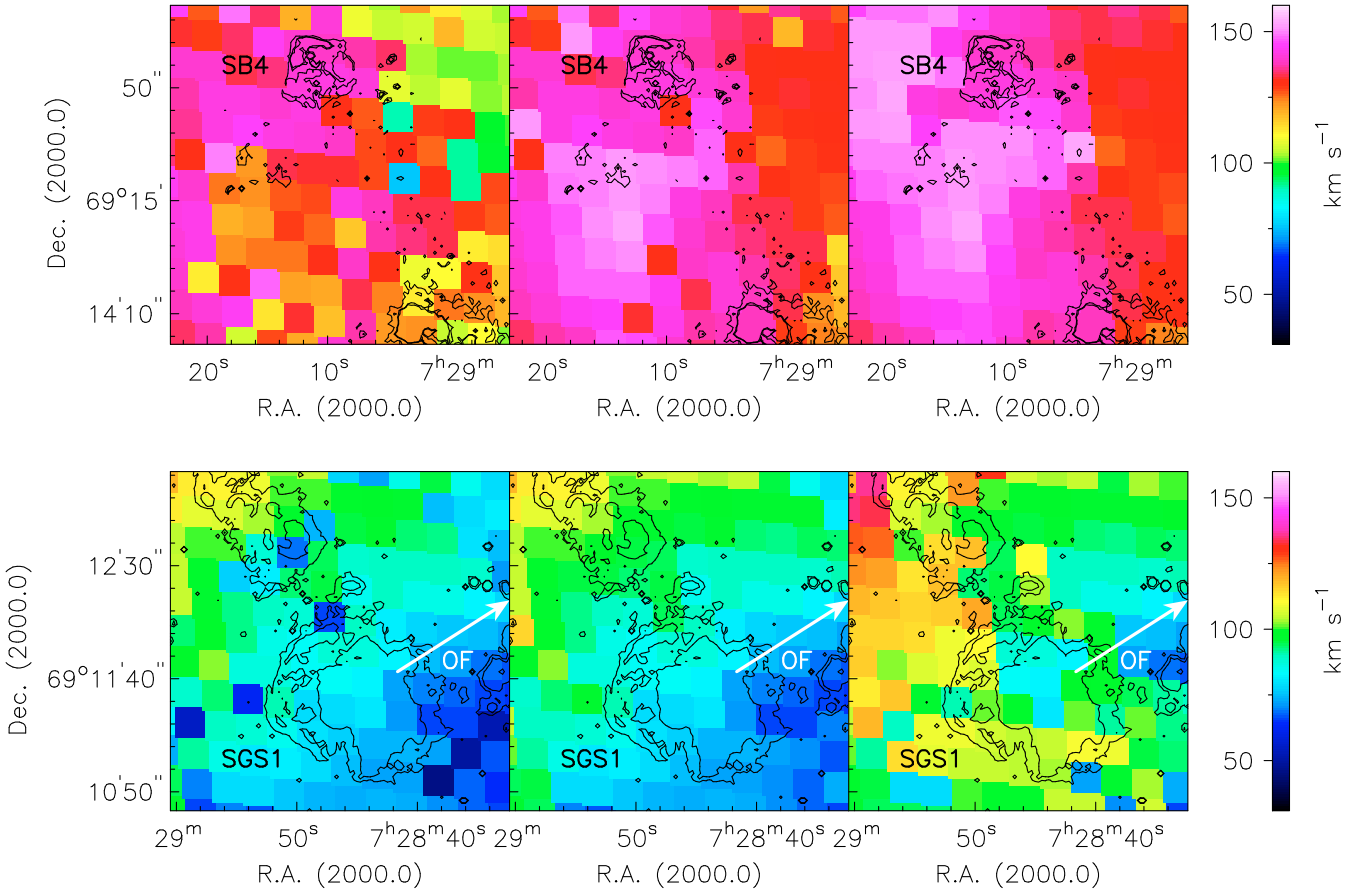

Fig. 10. The same as Fig. 8 for two peculiar areas in the central region of NGC 2366. The *upper row* shows the superbubble SB4 and its surroundings, the *lower row* presents the GEHR and the onset of the northern tail. Again, the three H I velocity components are plotted. Overlaid are the Hα intensity contours. The superbubble SB4, the supergiant shell SGS1 (see van Eymeren et al. 2007) and the outflow OF are marked.

dark matter dominated, we can calculate the escape velocities from dark matter halo models. There are two main competing models which describe the density distribution (and therefore the appearance of the rotation curve) in a dark matter dominated galaxy, the NFW model derived from Cold Dark Matter simulations (e.g., Navarro et al. 1996; Moore et al. 1998, 1999) which predicts a cuspy core, and the empirically derived pseudo-isothermal (ISO) halo (Binney & Tremaine 1987) predicting a core of constant density. This disagreement between simulations and observations, the so-called cusp-core discrepancy has been discussed in many publications during the last decade (e.g., de Blok & Bosma 2002). Recent studies have shown that the rotation curves of dwarf and low surface brightness galaxies can indeed better be described by an ISO halo, at least in the inner few kpcs (Kuzio de Naray et al. 2008; Spano et al. 2008).

As the detected outflows are all closely located to the dynamical centre of NGC 2366, we decided to model the escape velocities by using the ISO halo. This decision was further supported by a mass decomposition which confirms that the rotation curve of NGC 2366 can better be described by the ISO halo (van Eymeren 2008). Its density profile is given by

$$\rho_{\rm ISO}(r) = \rho_0 \left(1 + \left(\frac{r}{r_{\rm c}}\right)^2\right)^{-1} \quad (1)$$

with ρ_0 being the central density and $r_{\rm c}$ the core radius. The escape velocity is then given by

$$v_{\rm esc}(r) = \sqrt{2\, v_{\rm c}^2 \left(1 + \log\left(\frac{r_{\rm max}}{r}\right)\right)} \quad (2)$$

with $v_{\rm c}$ being the circular velocity and $r_{\rm max}$ being the maximum radius of the dark matter halo (see Binney & Tremaine 1987).

We plotted the resulting escape velocities in Fig. 12. The H I rotation curve including receding and approaching side is indicated by small grey triangular-shaped symbols. The expanding gas structures are marked by black large triangles. We corrected the values for an inclination of 64° as calculated in Sect. 4.2, which leads to an increase in velocity of about 10%. The circular velocity was measured from the rotation curve to be 50 km s^{-1} (see Table 1). We plotted the escape velocity for two different radii $r_{\rm max}$ = 7.5 kpc (dotted line) and $r_{\rm max}$ = 15 kpc (solid line). The lower value of $r_{\rm max}$ was chosen to equal the size of the H I outer radius. This is the outermost point where we can directly measure a contribution of dark matter from the rotation curve, which gives us therefore a lower limit for the radius of the dark matter halo. Most probably, the dark matter halo is much larger so that we chose the second value to be twice the size of the H I radius (which might still be too small). Nevertheless, a higher $r_{\rm max}$ increases the escape velocities, which means that all radii greater than the H I radius decrease the probability of a galactic

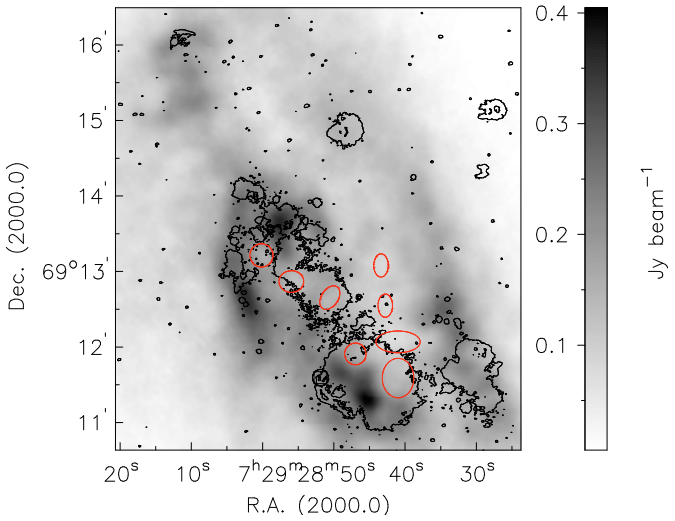

Fig. 11. The locations of the central H I holes in NGC 2366. The inner part of the H I intensity distribution is shown. In order to facilitate the comparison of the locations of the H I holes (indicated by red (light grey) ellipses) with the ones of the outflows, the outer Hα contour is displayed in black.

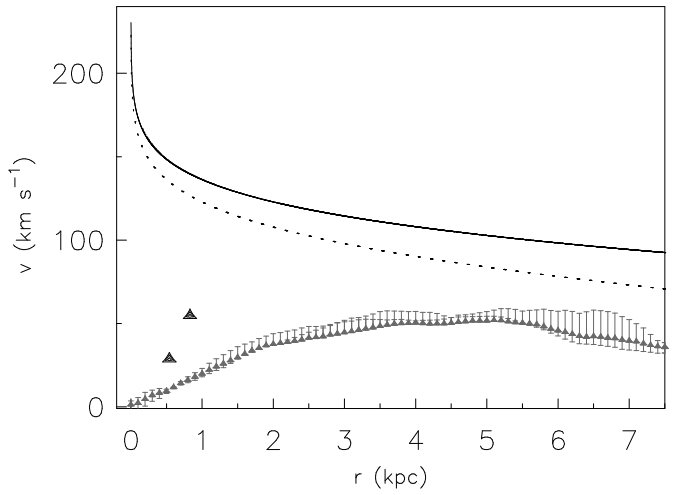

Fig. 12. Escape velocity for a pseudo-isothermal halo of r_{max} = 7.5 kpc (dotted line) and r_{max} = 15 kpc (solid line). The observed rotation curve is indicated by small grey triangles. The error bars represent receding and approaching side. The expanding gas structures are marked by black large triangles.

wind so that the H I radius can indeed be regarded as a lower limit for the escape velocity.

Figure 12 shows that both outflows have expansion velocities that lie clearly below the escape velocity. As the ISO halo is characterised by a core of constant density, the escape velocities in the inner parts are even higher than by using a rapidly decreasing NFW density profile. This result is in good agreement with hydrodynamic simulations (Mac Low & Ferrara 1999, see Sect. 1). With a gas mass of about 10^9 $M_\odot$ NGC 2366 is located at the upper end of the mass distribution simulated by Mac Low & Ferrara (1999). This means that according to their simulations, a blow-away of gas is very unlikely. Nevertheless, the escape velocity drops significantly at greater distances from the dynamic centre, which enhances the probability of a galactic wind for gas in the halo. However, the deep Hα image of NGC 2366 shows no filamentary or shell-like structures at several kpcs from the disc. Either the emission is too weak to be detected or the gas has not managed so far to expand to such large distances.

6. Summary

Optical images, Fabry-Perot interferometric data, and H I synthesis observations were used to get new insights into the morphology and the kinematics of the neutral and ionised gas components in the nearby irregular dwarf galaxy NGC 2366. The most important results are shortly summarised here.

In agreement with recent studies we suggest the existence of two weak spiral arms in NGC 2366.

The galaxy harbours two major outflows detected in the Hα velocity field. The large red-shifted outflow has an expansion velocity of 50 km s^{-1}. The FP data allowed us for the first time to measure the whole extent of this outflow. With a length of 1.4 kpc it is one of the largest outflows found so far in a dwarf galaxy. This outflow as well as the supergiant shell SGS1 and the superbubble SB4 do not have any counterpart in H I and they all expand into an area of low H I column density. We therefore suggest that major parts of the gas have already been ionised. The second outflow is located north of the GEHR NGC 2363 and expands with 30 km s^{-1} blue-shifted. It is also visible in H I. Several nearby small H I holes show that a fraction of the neutral gas has already been ionised or blown away. An estimation of the expansion ages reveals that the current star clusters are probably not the first drivers of the outflows or that the gas is slowed down which decreases the chance for a galactic wind.

We compared the measured expansion velocities with the escape velocities of the galaxy, calculated from a pseudo-isothermal halo model. In both cases and independent of the choice of r_{max}, the expansion velocities of the outflows stay far below the escape velocity, which means that the gas is still gravitationally bound and would need an event like a SN explosion to be accelerated to the escape velocity. Our result is in agreement with hydrodynamic simulations and draws therefore our attention to less massive galaxies.

Acknowledgements. The authors would like to thank Fabian Walter and the THINGS team for providing the reduced H I data cube of NGC 2366.
This work was partly supported by the Deutsche Forschungsgesellschaft (DFG) under the SFB 591, by the Research School of the Ruhr-Universität Bochum, and by the Australia Telescope National Facility, CSIRO. It is partly based on observations collected at the Observatoire de Haute-Provence and at the Centro Astronómico Hispano Alemán (CAHA) at Calar Alto, operated jointly by the Max-Planck Institut für Astronomie and the Instituto de Astrofísica de Andalucía (CSIC). We made use of NASA's Astrophysics Data System (ADS) Bibliographic Services and the NASA/IPAC Extragalactic Database (NED) which is operated by the Jet Propulsion Laboratory, California Institute of Technology, under contract with the National Aeronautics and Space Administration.
Last but not least we would like to thank the anonymous referee for his suggestions which helped to improve this paper.

Appendix A: Hα image and extension of the catalogue of ionised gas structures

Here, the continuum-subtracted Hα image is again presented in an enlarged version and with a different contrast as in Fig. 1 to emphasise the faint and diffuse ionised gas structure (see Fig. A.1). The isolated H II regions as well as the new detections of shell-like material are marked and numbered. The positions of the potential spiral arms are indicated. Additionally, an extension of the catalogue by van Eymeren et al. (2007) is presented in Table A.1.

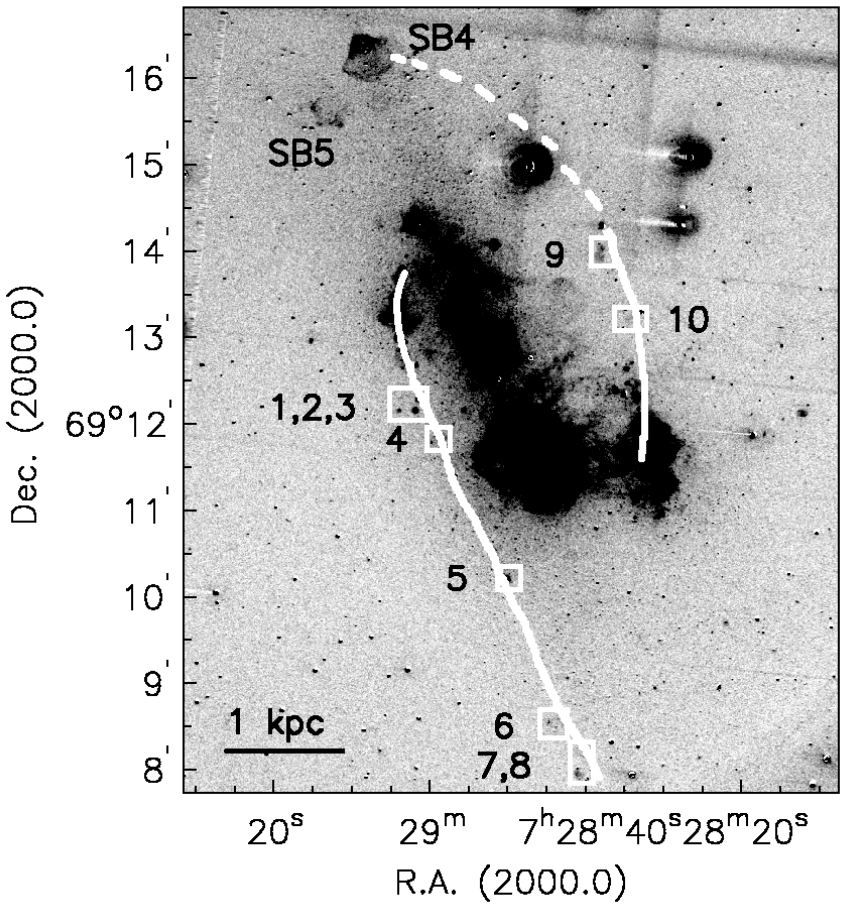

Fig. A.1. Continuum-subtracted Hα image of NGC 2366. The contrast is chosen in a way to demonstrate the large-scale structures. The extraplanar H II regions are marked by white boxes and numbered in black. Additionally, the two northern superbubbles are numbered following van Eymeren et al. (2007). The positions of the spiral arms are indicated by white lines.

Table A.1. The most prominent structures and their sizes in NGC 2366 – an extension.

Source	Diameter [″]	Diameter [pc]	$v_{\rm helio}$ [km s^{-1}]	*FWHM* [km s^{-1}]
SB4	30	500	...	...
SB5	25	417	...	...

References

Binney, J., & Tremaine, S. 1987, Galactic dynamics (Princeton, NJ: Princeton University Press), 747
Bomans, D. J., Chu, Y., & Hopp, U. 1997, AJ, 113, 1678
Chu, Y., & Kennicutt, R. C. 1994, ApJ, 425, 720
de Blok, W. J. G., & Bosma, A. 2002, A&A, 385, 816
de Vaucouleurs, G., de Vaucouleurs, A., Corwin, H. G., et al. 1991, Third Reference Catalogue of Bright Galaxies (Berlin, Heidelberg, New York: Springer-Verlag), Vol. 1–3, XII, 2069
Drissen, L., Roy, J.-R., Robert, C., Devost, D., & Doyon, R. 2000, AJ, 119, 688
Drissen, L., Crowther, P. A., Smith, L. J., et al. 2001, ApJ, 546, 484
Gach, J.-L., Hernandez, O., Boulesteix, J., et al. 2002, PASP, 114, 1043
Gil de Paz, A., & Madore, B. F. 2005, ApJS, 156, 345
Hodge, P., Kennicutt, R. C., & Strobel, N. 1994, PASP, 106, 765
Hunter, D. A., & Elmegreen, B. G. 2006, ApJS, 162, 49
Hunter, D. A., & Gallagher, J. S. 1997, ApJ, 475, 65
Hunter, D. A., Hawley, W. N., & Gallagher, J. S. 1993, AJ, 106, 1797
Hunter, D. A., Elmegreen, B. G., & van Woerden, H. 2001, ApJ, 556, 773
Kuzio de Naray, R., McGaugh, S. S., & de Blok, W. J. G. 2008, ApJ, 676, 920
Mac Low, M., & Ferrara, A. 1999, ApJ, 513, 142
Martin, C. L. 1998, ApJ, 506, 222
Moore, B., Governato, F., Quinn, T., Stadel, J., & Lake, G. 1998, ApJ, 499, L5
Moore, B., Quinn, T., Governato, F., Stadel, J., & Lake, G. 1999, MNRAS, 310, 1147
Navarro, J. F., Frenk, C. S., & White, S. D. M. 1996, ApJ, 462, 563
Norman, C. A., & Ikeuchi, S. 1989, ApJ, 345, 372
Richter, G. M., Lorenz, H., Bohm, P., & Priebe, A. 1991, Astron. Nachr., 312, 345
Roy, J., Boulesteix, J., Joncas, G., & Grundseth, B. 1991, ApJ, 367, 141
Shapiro, P. R., & Field, G. B. 1976, ApJ, 205, 762
Slavin, J. D., Shull, J. M., & Begelman, M. C. 1993, ApJ, 407, 83
Spano, M., Marcelin, M., Amram, P., et al. 2008, MNRAS, 383, 297
Stevens, I. R., & Strickland, D. K. 1998, MNRAS, 301, 215
Thuan, T. X., & Martin, G. E. 1981, ApJ, 247, 823
Thuan, T. X., Hibbard, J. E., & Lévrier, F. 2004, AJ, 128, 617
Tikhonov, N. A., & Galazutdinova, O. A. 2008, Astron. Rep., 52, 19
Tolstoy, E., Saha, A., Hoessel, J. G., & McQuade, K. 1995, AJ, 110, 1640
van Eymeren, J. 2008, Ph.D. Thesis, Astronomisches Institut der Ruhr-Universitaet Bochum, Germany
van Eymeren, J., Bomans, D. J., Weis, K., & Dettmar, R.-J. 2007, A&A, 474, 67
Walter, F., Brinks, E., de Blok, W. J. G., et al. 2008, ArXiv e-prints
Wilcots, E. M., & Thurow, J. C. 2001, ApJ, 555, 758